Heliyon 7 (2021) e07451

Contents lists available at ScienceDirect

Heliyon

journal homepage: www.cell.com/heliyon

Research article

Integration of heterogeneous photocatalysis and persulfate based oxidation using TiO_2-reduced graphene oxide for water decontamination and disinfection

Deepthi John [a,b,*], Jiya Jose [c], Sarita G. Bhat [c], V. Sivanandan Achari [a,**]

[a] School of Environmental Studies, Cochin University of Science and Technology, Kochi, 682022, Kerala, India
[b] Department of Chemistry, Deva Matha College, Kuravilangad, 686633, Kerala, India
[c] Department of Biotechnology, Cochin University of Science and Technology, Kochi, 682022, Kerala, India

ARTICLE INFO

Keywords:
Advanced oxidation process
Persulfate oxidation
Photocatalysis
TiO_2-Reduced graphene oxide nanocomposites
Antibacterial properties
Cytotoxic analysis

ABSTRACT

Advanced oxidation processes (AOPs) which involve the generation of highly reactive free radicals have been considered as a promising technology for the decontamination of water from chemical and bacterial pollutants. In this study, integration of two major AOPs *viz*., heterogeneous photocatalysis involving TiO_2-reduced graphene oxide (T-RGO) nanocomposite and activated persulfate (PS) based oxidation was attempted to remove diclofenac (DCF), a frequently detected pharmaceutical contaminant in water. The enhanced visible light responsiveness of T-RGO would facilitate the use of direct sunlight as a benign and cost effective source of energy for the photocatalytic activation. By combining PS based oxidation process with T-RGO mediated photocatalysis, a DCF removal efficiency of more than 98% was achieved within 30 min. The effect of operating parameters like PS concentration and pH on DCF removal was assessed. Radical scavenging experiments indicated that apart from radical oxidation involving $^{\bullet}OH$ and $SO_4^{\bullet-}$ radicals, a non-radical oxidation pathway was also taking place in the degradation. The antibacterial properties of the integrated system were also evaluated using *Escherichia coli* and *Staphylococcus aureus* as representative bacteria. The presence of PS in the photocatalytic reaction system improved the antibacterial activity of the composite against the two strains studied. Cytotoxicity of T-RGO nanocomposite was assessed using human macrophage cell lines and the results showed that the composite is biocompatible and nontoxic at the recommended dosage for water treatment in the present study.

1. Introduction

The development of new water treatment methods has gathered momentum nowadays due to the many fold increase in the contamination of water that we use in everyday life. Among the several methods, advanced oxidation processes (AOPs) have been considered as an emerging technology as it involves the generation of highly reactive free radicals especially hydroxyl ($^{\bullet}OH$) radicals which could completely mineralise the pollutants. Among various AOPs, heterogeneous photocatalysis using graphene based semiconductor metal oxides, mainly TiO_2, and sulfate radical based AOPs (SR-AOPs) have attracted a lot of attention in recent years due to their widespread applicability and enhanced efficiency in degrading pollutants from water. TiO_2 is an established photocatalyst for wastewater detoxification [1]. However, its photocatalytic efficiency is still limited by the high rate of electron-hole pair recombination. Incorporation of graphene in TiO_2 enhances the photocatalytic activity due to the high ability of graphene to accept/transport the photogenerated electrons, thus decreasing the electron-hole recombination. Besides, the addition of graphene to TiO_2 extends light absorption range to visible light region and also improves the surface properties and chemical stability, making it a highly promising photocatalyst.

The two common oxidants used in SR-AOPs are persulfate (PS, $S_2O_8^{2-}$) and peroxy monosulfate (PMS, HSO_5^-). Of these, PS is the better choice due to its stability at ambient temperature, excellent aqueous solubility, high oxidation potential and comparatively low cost [2]. Being stable at ambient temperature external activation is imperative for PS oxidation. PS contains a symmetric O–O bond of length 1.497 A^0 and energy 140 kJ/mol [3] and the fundamental mechanism of activation involves the breaking of

* Corresponding author.
** Corresponding author.
E-mail addresses: deepthi.john@devamatha.ac.in (D. John), vsachari@cusat.ac.in (V.S. Achari).

https://doi.org/10.1016/j.heliyon.2021.e07451
Received 31 October 2020; Received in revised form 15 March 2021; Accepted 28 June 2021

this bond to form highly reactive sulfate ($SO_4^{\bullet-}$) radical anions. $SO_4^{\bullet-}$ radical anions have high selectivity and equal or higher oxidation potential (2.5–3.1 V) compared to $^{\bullet}OH$ radicals (2.8 V) [4]. Various strategies such as heat, ultrasound, UV irradiation, transition metals, metal oxides, bases and carbonaceous materials are employed [5] for PS activation. Among these, heterogeneous activation involving metal oxide semiconductors has played a significant role in PS activation [6]. The activation of PS by carbocatalysts like activated carbon [7], mesoporous carbon [8], RGO [9] and GO/TiO_2 nanosheet [10] has also been reported recently. In the case of RGO activation it was reported [11] that the π-conjugated graphitic domains with defective edges as well as the oxygen functional groups (mainly C=O groups) present on the surface might be the active catalytic sites for PS activation.

The electron rich environments in graphene together with the defective edges are supposed to weaken and break the –O-O- bond to generate sulfate radicals. Though, TiO_2-reduced graphene oxide (T-RGO) nanocomposite has been recognised as one among the most successful modifications of TiO_2 in terms of photocatalytic efficiency, the ability of this catalyst to activate PS has not been reported so far. In the present work, the better photocatalytic performance of T-RGO along with the potential of RGO to activate PS has been explored for the removal of diclofenac (DCF).

For the practical application of any process factors such as cost effectiveness, impact on environment, feasibility for large scale use etc. have to be considered. Among the various PS activation methods, heat/US/UV etc. will demand high cost and energy input. Homogeneous activation by metal ions may also raise some serious issues like precipitation of metal ions at low pH, the formation of hydrated species at high pH, leaching of metal ions; all these would require substantial increase in metal loading to make up the loss and to sustain the efficiency. This would need an additional treatment step to remove the excess additives from the treated water, further raising treatment cost. The adverse health impacts on humans by some metal ions like cobalt are also a matter of serious concern. In this regard two promising AOPs *viz.*, heterogeneous photocatalysis and PS-based AOPs could be integrated with T-RGO as it would play the dual role of a photocatalyst and a PS activator. Besides, T-RGO was reported to be more stable, easily separable and efficiently recyclable [12, 13, 14]. The improved visible light absorption of T-RGO would enable the use of direct sunlight as a benevolent and cost effective light source for activation.

The eradication of pathogenic microorganisms from water through photocatalytic inactivation has also been identified as a guaranteed mechanism recently, as it can be applied without the formation of any disastrous by-products under light irradiation. For the successful nullification of pathogenic bacteria, photocatalysis using TiO_2 had been largely administered for disinfection during the previous decades. In recent years, the antimicrobial properties of graphene based nanocomposites have attracted a lot of attention in the field of photocatalytic wastewater treatment and researchers have been interested in improving their antimicrobial activity. In this study, the suitability of the said integrated process towards photocatalytic inactivation has also been evaluated by taking two representative bacteria *viz.*, *Escherichia coli*, a gram-negative and the most commonly found bacterium in water bodies and *Staphylococcus aureus*, a gram-positive bacterium usually found in upper respiratory tract and on the skin of human beings.

This study aims to investigate the effectiveness of combining heterogeneous photocatalysis and PS- based AOPs, under sunlight for the degradation of DCF. Optimum experimental conditions for DCF removal are established. A probable mechanism is proposed on the basis of radical scavenging experiments. The antibacterial properties of T-RGO/PS system towards the photocatalytic inactivation of *E. coli* and *S. aureus* are also evaluated. Further, the cytotoxicity effect of T-RGO catalyst is evaluated using human macrophage cell lines to assess its safe use in water treatment.

2. Materials and methods

2.1. Materials

Titanium (IV) isopropoxide for the synthesis of T-RGO was procured from Sigma Aldrich, India. Graphite powder and diclofenac sodium were purchased from Alfa Aesar, India. Potassium persulfate was obtained from Qualigens, India. $KMnO_4$ and various solvents were from Merck, India and used without further purification.

2.2. Synthesis and characterization of T-RGO nanocomposite

Graphene Oxide (GO) was synthesised by modified Hummer's method. T-RGO nanocomposite with 5w/w ratios of GO was prepared by solvothermal treatment of titanium isopropoxide and GO in isopropanol (details of the methodology used for the synthesis of TiO_2, T-RGO and RGO are given in Supplementary Material). The prepared catalysts were characterized by various analytical techniques. X-ray diffraction (XRD) analysis was done using Bruker AXS D8 diffractometer employing Cu Kα radiation (1.5418 Å) with a Ni filter and at a scan rate of 0.5°/min. Thermo NICOLET 380 Fourier transform infrared (FTIR) instrument was used for FTIR measurements by making KBr disks containing sample. Spectra were taken in the transmission mode with a resolution of 4 cm^{-1} in the range of 4000–400 cm^{-1}. X-ray photoelectron spectroscopy (XPS) analysis was made with Axis Supra (XPS) surface analysis instrument using a monochromatic Al Kα radiation. Raman spectra were acquired using a confocal microprobe Raman system (WITec alpha300RA) with an excitation wavelength of 532 nm from a He–Ne laser. Photo luminescence spectra (PL) were obtained with a Shimadzu model RF-5301PC spectrofluorophotometer. Diffuse Reflectance spectra (DRS) were obtained by Jasco V-570 UV-Vis spectrophotometer taking $BaSO_4$ as reference at a scanning speed of 100 nm/min and bandwidth of 5.0 nm. Transmission Electron Microscopy (TEM) images were taken using Jeol/JEM-2100 operated at an acceleration voltage of 200 kV. The specific surface area and pore size distribution were acquired from nitrogen sorption isotherms on a Micromeritics Tristar 3000 V6.07A surface area and porosity analyser. The synthesis procedure and detailed discussion on the characterization of T-RGO nanocomposite have been reported elsewhere [14, 15].

2.3. Solar photocatalytic experimental procedure

Solar photocatalytic experiments were conducted in a specially designed jacketed pyrex glass reactor. In a typical experiment 50 mL of 25 mg/L DCF solution, 75 mg/L of the catalyst and 20 mg/L of PS were stirred in the dark for 1 h to attain adsorption-desorption equilibrium. This solution was then introduced into the inner compartment of the reactor. Cooling water from a thermostat was circulated through the jacket to keep the temperature constant (27 ± 1 °C). The experiments were conducted at Kochi, Kerala, India with an average light intensity of 1.25×10^5 lx. DCF concentration was monitored spectrophometrically (274.6 nm) and by measuring total organic carbon (TOC) at regular time intervals.

The photodegradation of DCF is calculated using Eq. (1) [16].

$$\% \text{ photodegradation} = [(C_0 - C) / C_0] \times 100 \quad (1)$$

where C_0 is the original DCF content, C is the DCF remaining in solution at time t.

2.4. Antibacterial studies

2.4.1. Antibacterial activity of T-RGO and T-RGO/PS integrated systems

The inherent antibacterial activity of the composite was ascertained qualitatively by the well diffusion method. Wells each having 6 mm

diameter was cut on the agar plate, inoculated with the test microorganism and 50 μL of each sample solution was carefully transferred to each well. This was kept for incubation at 37 °C for a period of 24 h. Thereafter the diameters of the inhibition zones were measured and optical images of the plates were taken.

The light sensitive antibacterial activities of the composite systems were studied quantitatively by the colony count method. In a typical experiment, each bacterial strains (~$10^{5\text{-}7}$ CFU/mL), in required volumes was taken in bottles containing catalyst (0.1 mg/mL) and PS (0.01 mg/mL). The mixtures were subsequently kept for incubation at 37 °C in a rotary shaker at 150 rpm and simultaneously irradiated using visible LED light of 455 nm and a power of 50 W. In the process of sampling at regular intervals of time, I mL of the experimental solution was pipetted out into 9 mL of sterile saline and serially diluted. Further 100 μL of each dilution was spread on a nutrient agar plate and the number of colonies was counted. The antibacterial activity was calculated using Eq. (2) [17].

$$\text{Antibacterial activity } \% = (N_t / N_0) \times 100 \quad (2)$$

Where N_0 and N_t are the viable cell counts before and after the irradiation respectively.

2.4.2. Bacterial morphology analysis using Atomic Force Microscopy (AFM)

Atomic Force Microscopy has been employed considerably during recent years as a standard tool for investigating the surface structure of samples at high resolution. This technique provides three dimensional topographies with atomic resolution in real time, under air, aqueous or vacuum conditions at a range of temperatures and with basic sample preparation (e. g., does not require dehydration, staining with dyes or surface coating with metals) [18, 19]. Therefore, AFM has good prospects over other microscopic techniques which use light and electron wavelengths in providing accurate two- and three-dimensional surface images with quantifiable and accurate surface height information.

The basic principle of AFM is the sensing of the force between a very sharp probe which is placed at the end of a flexible cantilever and the sample surface. Thus an AFM image is generated by recording the very weak interatomic interactions between the sample surface and the probe tip as the probe is scanned over the sample surface.

A number of AFM imaging modes are available and the selection of a suitable imaging mode depends on the characteristics of the sample to be tested [19]. For soft biological samples tapping mode AFM is preferred as the samples are less likely to be damaged by the tip. In this mode, the cantilever of the probe is excited to a mechanical oscillation near its resonance frequency, and the probe makes contact with the sample intermittently. The interaction of the tip with the sample surface causes a change in the amplitude of oscillation and by adjusting the position of the sample or the cantilever, the amplitude as well as the force between the probe and the sample can be kept constant. Changes in the position of the sample or the cantilever are monitored and displayed as AFM images [20, 21]. A notable advantage of using the tapping mode is that it effectively eliminates the influence of the lateral force, resulting in images with excellent lateral resolution. Further, the damage to the sample is largely avoided so that its original appearance can be produced precisely.

In this study the morphological changes of the cells before and after photocatalytic treatment were evaluated using WITec alpha300RA AFM instrument. The measurements were carried out in tapping mode with silicon tip of 75 kHz resonant frequency and 2.8 N/m force constant. 2 mL each of control and treated *E. coli* and *S. aureus* suspensions were collected, washed several times with deionized water to remove the adherent nanoparticles and centrifuged. The final pellet was applied individually to the surface of glass slides and dried at room temperature prior to analysis. The sample was focused by an optical Zeiss objective (20X Zeiss microscope) with numerical aperture 0.4. The acquired AFM images were processed and analysed using control 4 program.

2.5. Toxicity assessment of T-RGO nanocomposite

2.5.1. MTT Cell Viability Assay

The MTT assay is used to measure cellular metabolic activity as an indicator of cell viability, proliferation and cytotoxicity. 3-(4,5-dimethylthiazol-2-yl)-2,5-diphenyl tetrazolium bromide (MTT) is a yellow dye, which is reduced by cellular enzymes to the blue product formazan. As the transformation is possible in viable cells only, the amount of blue formazan formed is proportional to the number of viable cells.

To evaluate the viability of cells grown with T-RGO, MTT assay was carried out using the human macrophage cell lines (Raw 264.7, ATCC, TIB-71). As per the instructions of the manufacturer (Thermo Fisher Scientific, USA), cells were grown in 96 well plates and treated with different volumes of 1 mg/mL of nanocomposite. After incubation, cells were treated with 100 μL of MTT dye solution and incubated at 37 °C for a period of 4 h. Thereafter, solvent dimethyl sulfoxide (DMSO) was added to dissolve the formazan crystals. Readings were taken at a wavelength of 570 nm. The absorbance was converted into cell viability (%) using Eq. (3) [22, 23].

$$\text{Cell viability } (\%) = \frac{OD \text{ of sample}}{OD \text{ of control}} \times 100 \quad (3)$$

where *OD* is the optical density for absorbance measurements.

2.5.2. Metabolic activity assay

Human macrophage cell lines were treated with T-RGO nanocomposite and the effect was studied with Invitrogen Live/Dead cell staining kit. Studies were conducted according to the instructions of the manufacturer. Treated cells were incubated for a period of 4 h and images were observed using fluorescent microscope (Olympus BX 51). The live and dead cells appeared as green and red in colour, respectively.

3. Results and discussion

3.1. Characterization of T-RGO

The high crystallinity and the exclusive anatase phase of both pristine TiO_2 and T-RGO composite are evident from the XRD pattern (Fig. S1, Supplementary Material). The incorporation of graphene reduced the crystallite as well as the particles sizes of TiO_2 (from a mean diameter of ~11 to ~4 nm) and a finer dispersion of TiO_2 onto layered 2D graphene can be observed from the TEM images (Figure 1). The reduced rate of electron-hole recombination in T-RGO compared to TiO_2 is obvious in the PL spectrum (Fig. S2, Supplementary Material). The specific surface area calculated from the Brunauer-Emmett-Teller (BET) method shows that surface area increases from 78 to 140 m^2/g on graphene incorporation. The catalysts show Type IV isotherm characteristic of mesoporous materials (Fig. S3, Supplementary Material). The pores are also in the mesoporous region (2–50 nm) with a narrow pore size distribution. Raman spectra of TiO_2 and T-RGO are shown in Figure 2. Vibration peaks at 140 cm^{-1} (E_g), 395 cm^{-1} (B_{1g}), 515 cm^{-1} (A_{1g}) and 639 cm^{-1} (E_g) correspond to the Raman active modes of anatase [24]. The characteristic D and G bands in the Raman spectra of T-RGO and GO are shown in the inset of Figure 2. The D band corresponds to sp^3 defects and disorders seen particularly along the edges of graphene sheets and G band is associated to in-plane vibrations of sp^2 carbon atoms [25]. The intensity ratio (I_D/I_G) calculated from Raman spectrum is a measure of disorder in carbonaceous materials. The higher I_D/I_G value of T-RGO (1.232) compared to GO (0.995) shows that T-RGO is formed with more number of edge planes and sp^3 defects.

The presence of oxygen containing functional groups like OH, C=O, and Ti–O–C bond is evident from FTIR (Fig. S4, Supplementary Material)

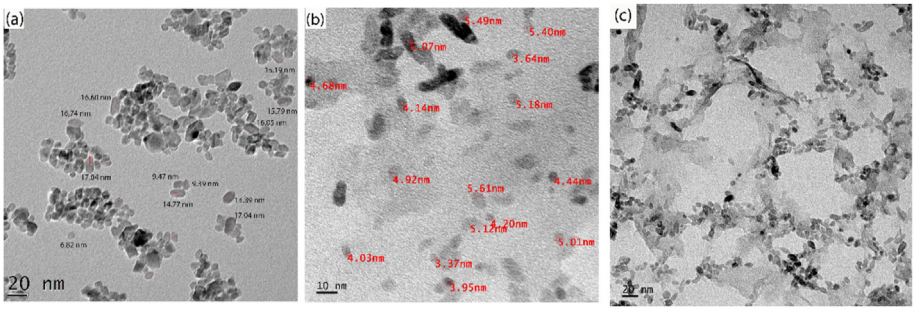

Figure 1. TEM images of (a) TiO_2 (b & c) T-RGO.

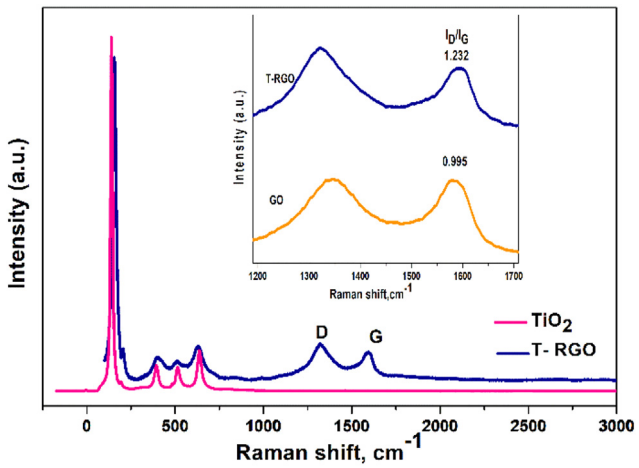

Figure 2. Raman spectra of TiO_2 and T-RGO. Inset characteristic D and G bands of GO and T-RGO.

and XPS spectra (Fig. S5a-d, Supplementary Material). The XPS survey spectrum of T-RGO (Fig. S5a) shows the existence of the elements Ti, O and C in the composite. XPS spectrum of Ti 2p (Fig. S5b) consists of two intense peaks for Ti $2p_{1/2}$ and Ti $2p_{3/2}$ centred at 463.6 and 458 eV with a spin-energy separation of 5.6 eV which corresponds to the binding energy values of Ti^{4+} in anatase TiO_2 [26]. Deconvolution spectra for C 1s (Fig. S5c) show a number of characteristic peaks; 283.7 (Ti–C), 284.6 (non-oxygenated aromatic C=C), 286.7 (C–O), 287.1 (C=O) and 288.7 eV (Ti–O–C) [27, 28]. O 1s spectrum consists of two peaks; the major peak at 529.6 eV corresponds to the lattice oxygen of TiO_2 crystal and the minor peak at 531.9 eV is related to the hydroxyl groups on the surface of RGO [28]. High degree of defects as well as oxygen containing functional groups identified in the composite are the favourable factors for PS activation.

Figure 3(a) shows the UV-DRS spectrum of T-RGO together with TiO_2. The extended absorption to visible region is evident in the UV-DRS spectrum. Compared to TiO_2, a significant decrease of the reflectance in the visible region is observed for T-RGO. The band gap calculated for T-RGO nanocomposite using Kubelka Munk plot [29, 30] (Figure 3b) shows a decrease from 3.2 eV (TiO_2) to 2.51 eV which also suggests an increased light absorption in the visible region.

3.2. Investigation on the degradation of DCF

The enhanced photocatalytic activity of T-RGO (containing 5 weight % GO) compared to synthesised TiO_2 towards the degradation of DCF under sunlight was established in our previous work [14]. Factors such as better adsorption of the substrate, enhanced light absorption, excellent mobility of charge carriers, increased production of reactive radicals etc. resulting from the incorporation of graphene in the composite can be accounted for this.

Figure 4 presents the degradation of DCF by various systems under study. In the absence of any catalyst and PS, the degradation of DCF is almost negligible indicating that DCF is quite stable under sunlight. PS alone in the dark has no effect on the degradation of DCF, though an appreciable degradation of ~18 % is observed under sunlight. This means that the activation of PS by sunlight is taking place to a substantial extent. PS enhances the degradation of DCF significantly in the case of T-RGO/PS system. The degradation is complete in just 30 min. Even under dark conditions, a moderate enhancement in % removal of DCF (from 11

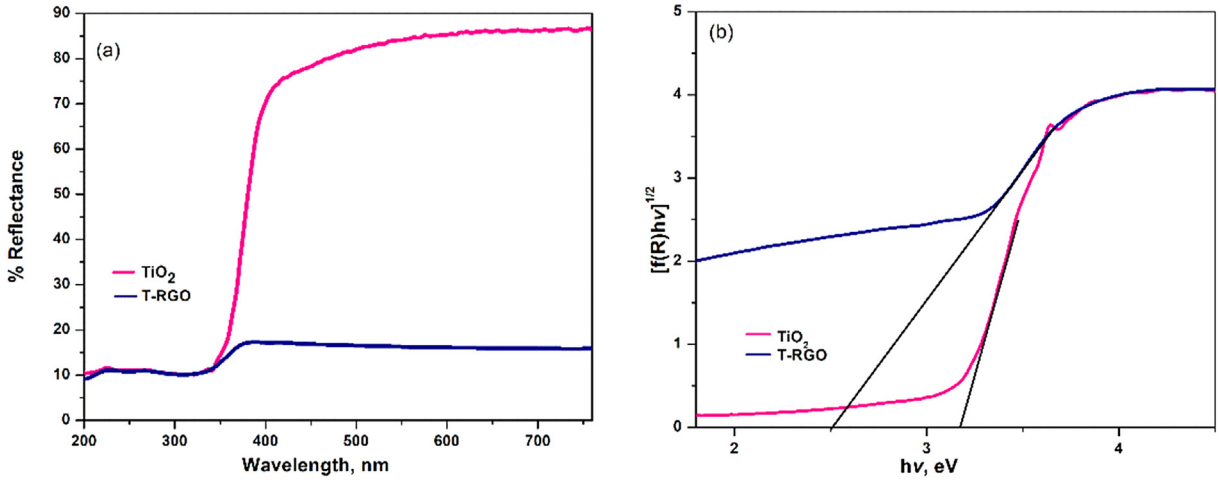

Figure 3. (a) UV-Vis diffuse reflectance spectra of TiO_2 and T-RGO. (b) A plot of transformed Kubelka Munk function versus the energy of light for TiO_2 and T-RGO.

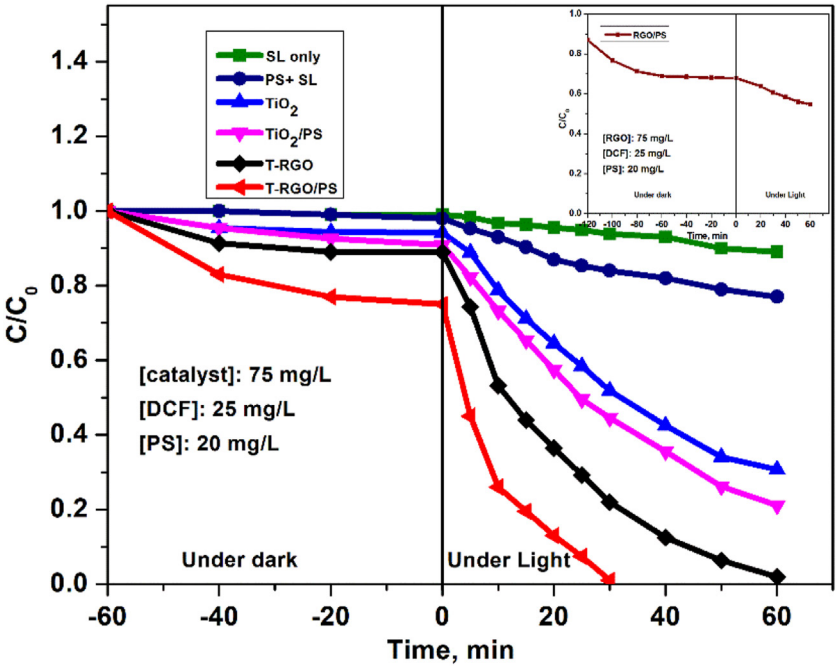

Figure 4. Degradation of DCF in sunlight over TiO_2, TiO_2/PS, T-RGO and T-RGO/PS.

to 25%) is observed on incorporating PS in the T-RGO system. The PS activation ability of T-RGO is evident here. PS also enhances the photocatalytic degradation of DCF by TiO_2, however the relative enhancement is less in this case. No significant difference is noticed under dark conditions irrespective of the addition of PS in the TiO_2 system. This implies that TiO_2 is not able to activate PS in the dark.

To further validate the PS activating ability of RGO, DCF removal efficiency in the RGO/PS system with the same catalyst/PS loadings has been investigated (Figure 4 inset). It has been found that RGO can activate PS in the dark and a removal efficiency of about 32% is observed and the rate becomes steady in 2 h. On subsequent sunlight illumination a further 15% degradation in 30 min is also noticed. These results illustrate the significant role of RGO in activating PS and in the subsequent degradation of DCF.

The degradation follows Langmuir– Hinshelwood mechanism and pseudo-first order kinetics as seen from the straight line logarithmic plots in Figure 5. The pseudo-first order rate constant, k_{app} calculated for T-RGO/PS system is 99.4 $\times 10^{-3}$ min^{-1} which is ~2 times than that for T-RGO (50.9 $\times 10^{-3}$ min^{-1}). This confirms that PS based oxidation is also taking place here and T- RGO plays an important role in PS activation under sunlight.

3.2.1. *Effect of persulfate (PS) concentration*

The amount of PS used in the process is a crucial factor as unused PS present in the water will contribute to sulfate toxicity and additional treatment for sulfate removal may increase the operation cost. Therefore, the dosage of PS needs to be optimised in such a way that the entire amount added is constructively utilised and no excess PS is present in the reaction system. Figure 6 shows the effect of PS concentration on the degradation of DCF. It is seen that as PS concentration increases the degradation increases and reaches an optimum at 20 mg/L and thereafter stabilizes/slightly increases.

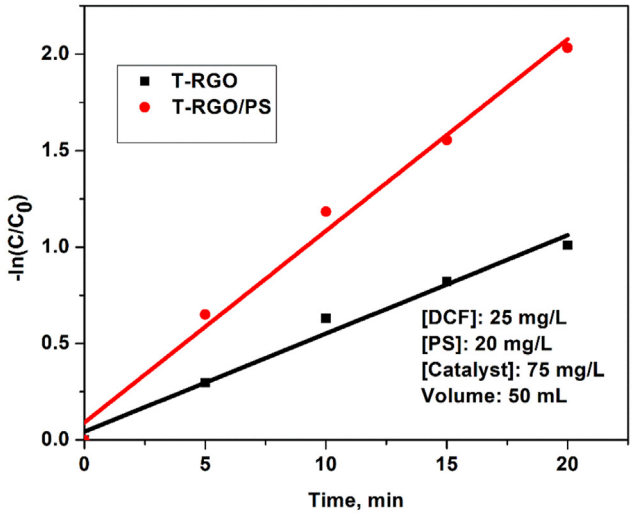

Figure 5. Logarithmic plot for the degradation of DCF in sunlight over T-RGO and T-RGO/PS.

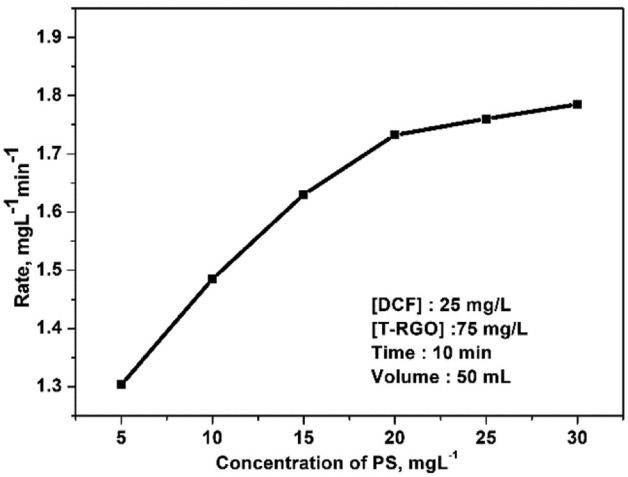

Figure 6. Effect of PS concentration on the degradation of DCF by T-RGO/PS system under solar light.

The enhancement of reaction rate in the presence of PS can be attributed to the facile formation of highly oxidising sulfate radical anion, $SO_4^{\cdot-}$, as in Eq. (4) [31]. This also leads to abstraction of electron and the resultant inhibition of electron-hole recombination. The sulfate radical anion will react with water molecule producing $^{\bullet}OH$ radical (Eq. 5) [31]. Both $SO_4^{\cdot-}$ and $^{\bullet}OH$ radicals participate in the degradation processes (Eqs. (6) and (7)).

$$S_2O_8^{2-} + e^- \rightarrow SO_4^{2-} + SO_4^{\cdot-} \quad (4)$$

$$SO_4^{\cdot-} + H_2O \rightarrow SO_4^{2-} + H^+ + \cdot OH \quad (5)$$

$$SO_4^{\cdot-} + RH \rightarrow SO_4^{2-} + \text{Intermediates} \quad (6)$$

$$\cdot OH + RH \rightarrow \text{Intermediates} \quad (7)$$

RH: Organic pollutant.

The breakage of SO-OS bond in PS and the subsequent formation of $SO_4^{\cdot-}$ depend largely on the binding energy of the bond and the capability of the catalyst to transfer electrons to the bond. In the presence of sunlight, the photogenerated electrons in TiO_2 will easily get transferred to the graphene layer. The π-conjugated electron system along with the high conductivity and the favourable work function of graphene facilitate this transfer which eventually lead to a highly electron rich behaviour in graphene. The electron rich graphene is able to break the O–O bond by modifying the electron density of the said bond. Thus the electron flowing environment in the graphene system will enhance the formation of $SO_4^{\cdot-}$.

It was reported that the C=O groups present on the defective edges of graphene would favour electron transfer thereby facilitating the formation of $SO_4^{\cdot-}$ as shown in Eq. (8) [32]. The electron transfer mechanism through oxygen functional groups like –COOH and –OH proposed in the case of activated carbon by Georgi and Kopinke [33] has been extended to the present system and shown as Eqs. (9) and (10).

$$rGO - C = O + S_2O_8^{2-} \rightarrow rGO - C - O^{\cdot} + 2SO_4^{\cdot-} \quad (8)$$

$$rGO - COOH + S_2O_8^{2-} \rightarrow rGO - COO^{\cdot} + SO_4^{\cdot-} + HSO_4^- \quad (9)$$

$$rGO - OH + S_2O_8^{2-} \rightarrow rGO - O^{\cdot} + SO_4^{\cdot-} + HSO_4^- \quad (10)$$

In the present study, the favourable factors for T-RGO for PS activation are the high degree of defects on the RGO structure as well as the oxygen containing functional groups identified in the composite. However, it can be observed that without illumination, the PS activation ability of T-RGO is less than that of RGO. It is reasonable to assume that some of the oxygen containing functional groups such as C=O, C–OH etc. are involved in Ti–O–C chemical bonding with TiO_2 which are not available for PS activation.

3.2.2. Effect of pH

pH plays a very significant role in the activation of PS thereby influencing the removal efficiency of DCF [5]. The effect of pH on the DCF degradation was examined by varying the pH from 3 to 11 (Figure 7). The natural pH of the DCF/T-RGO/PS system under optimised conditions was found to be 5.5. The maximum degradation is observed in the pH range of 4–6. This can be attributed to the increased production of $SO_4^{\cdot-}$ at acidic pH as shown in Eqs. (11) and (12). A similar result was reported by Genc et al. [10] also. When the pH is further decreased to 3 the degradation decreases. It was proposed by many authors [34] that at low pH the H^+ ion scavenges $SO_4^{\cdot-}$ according to Eq. (13). At pH > 6, again the degradation decreases slightly. This can be attributed to the reaction of $SO_4^{\cdot-}$ with water/OH^- and the corresponding scavenging occurs (Eqs. (14) and (15)). There is a possibility for the recombination of $SO_4^{\cdot-}$ and $^{\bullet}OH$ (Eq. 16) [35]. However, it is noted that an appreciable degradation is occurring at all pH showing that the system works at all pH ranges studied.

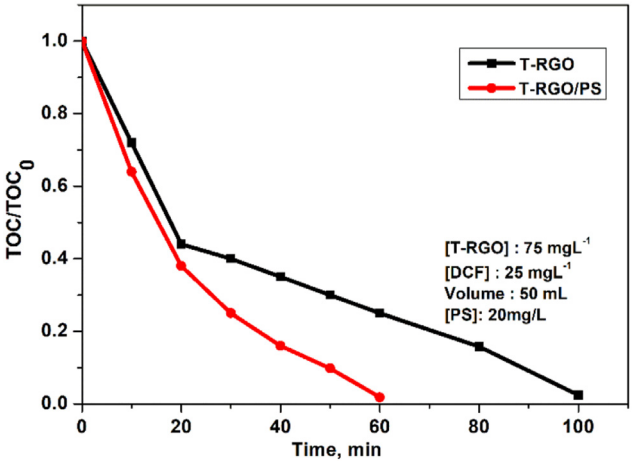

Figure 8. Decrease in TOC during the photocatalytic degradation of DCF with T-RGO and T-RGO/PS.

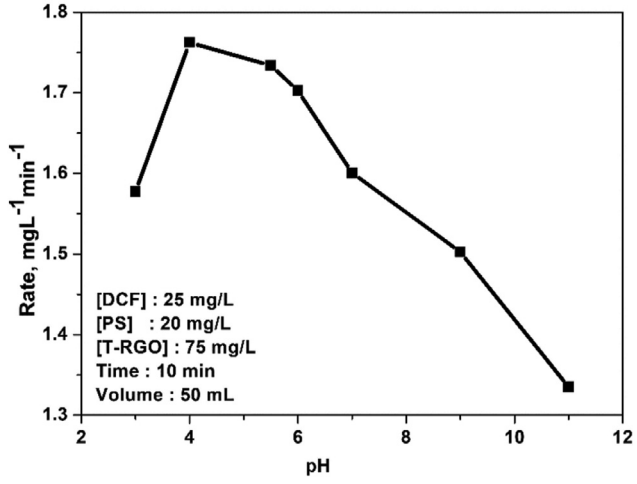

Figure 7. Effect of pH on the degradation of DCF by T-RGO/PS system under solar light.

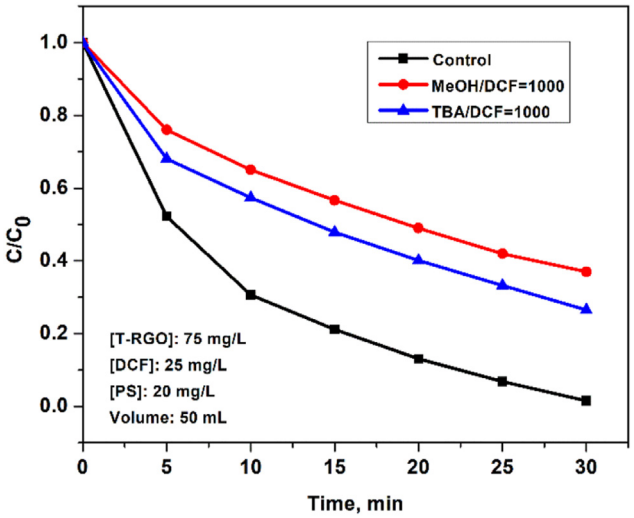

Figure 9. Effect of MeOH and TBA on DCF degradation.

$$S_2O_8^{2-} + H^+ \rightarrow HS_2O_8^- \quad (11)$$

$$HS_2O_8^{2-} + H^+ \rightarrow SO_4^{2-} + H^+ + SO_4^{\cdot-} \quad (12)$$

$$SO_4^{\cdot-} + H^+ + e^- \rightarrow HSO_4^- \quad (13)$$

$$SO_4^{\cdot-} + OH^- \rightarrow SO_4^{2-} + \cdot OH \quad (14)$$

$$SO_4^{\cdot-} + H_2O \rightarrow HSO_4^- + \cdot OH \quad (15)$$

$$SO_4^{\cdot-} + \cdot OH \rightarrow SO_4^{2-} + OH^- \quad (16)$$

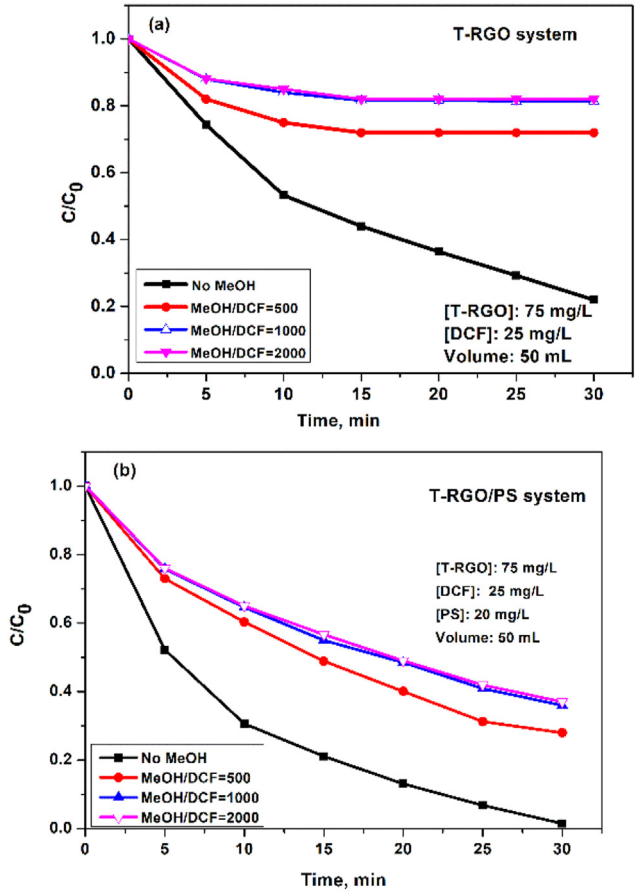

Figure 10. Effect of MeOH on DCF degradation (a) T-RGO (b) T-RGO/PS.

The maximum degradation between pH 4–6 can also be accounted for on the basis of pH dependent physico-chemical properties of the catalyst and the substrate. The pH_{PZC} of T-RGO as determined by the standard procedure [36] is 4.59 (Fig. S6, Supplementary Material) and accordingly the surface would be negative and attract cationic species above this pH and positive below this pH. The pKa value of DCF in water is 4.15 and it exists as a neutral species below this pH and as a negative ion above pH 4.15. If the adsorption due to electrostatic attraction of the negatively charged species (DCF and persulfate anions) on the catalyst surface and the subsequent degradation is considered as the major factor behind the DCF removal process, the degradation would be maximum between 4 and 4.59. The maximum degradation noted at pH 4 can also be accounted in the same way. However, the reasonable degradation rate observed throughout the pH range indicates that in addition to surface promoted decay process, degradation is also happening in the bulk of the solution due to the reaction between reactive oxygen species (ROS) and substrate as well as intermediates formed during the course of the reaction. Therefore, a multitude of factors like operational pH changes, ROS concentrations on the surface as well as in the bulk of the solution, surface charges of catalyst and substrates, ionic charges of the intermediate species formed, and the various possible interactions among these are to be considered and each reaction system needs to be configured accordingly.

3.2.3. Mineralisation of DCF

In order to ensure complete mineralisation of DCF, TOC was determined at regular intervals of irradiation. The results plotted in Figure 8 shows that T-RGO/PS system is more effective for the mineralisation compared to T-RGO. Continued irradiation reduces the TOC which eventually becomes nil after 1 h in the case of T-RGO/PS system.

3.2.4. Effect of radical scavengers

$^{\bullet}OH$ and $SO_4^{\cdot-}$ radical anions are considered as the major reactive species involved in contaminant oxidation in PS activated processes. To investigate the generation of these radicals and to distinguish their contribution in the degradation of DCF, quenching experiments with two radical scavengers, methanol (MeOH) and *ter*-butyl alcohol (TBA),

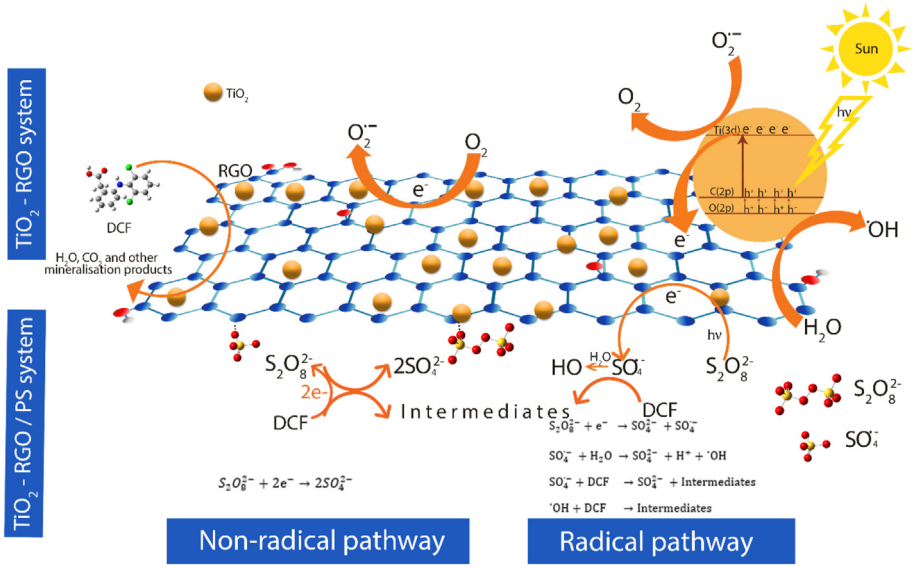

Figure 11. Graphical representation of the photocatalytic degradation of DCF by T-RGO/PS.

having different reactivity towards the said radical species were conducted. Methanol react with both $^{\bullet}OH$ and $SO_4^{\bullet-}$ at higher and comparable rate constants ($k_{\bullet OH} = 9.7 \times 10^8\ M^{-1}s^{-1}$, $k_{SO_4^{\bullet-}} = 1.1 \times 10^7\ M^{-1}s^{-1}$) and can be used as a scavenger for both the radicals [11]. On the other hand, TBA reacts more readily with $^{\bullet}OH$ ($k_{\bullet OH} = 6 \times 10^8\ M^{-1}s^{-1}$) but at a much lower rate with $SO_4^{\bullet-}$ ($k_{SO_4^{\bullet-}} = 4 \times 10^5\ M^{-1}s^{-1}$) and is usually employed to scavenge $^{\bullet}OH$ radicals only [8]. As displayed in Figure 9, the addition of TBA decreases the degradation of DCF to 72% while MeOH addition decreases the degradation to 63% in 30 min implying that both $SO_4^{\bullet-}$ and $^{\bullet}OH$ are generated and contributed significantly in the reaction. Further it can be inferred that the $^{\bullet}OH$ radicals are relatively more dominant than $SO_4^{\bullet-}$ radicals in the oxidation process. However, a significant removal efficiency is still achieved reflecting that there is non-radical oxidation which could continue the degradation even during the capture of radicals. Many authors [8, 37] have proposed non-radical oxidation pathways in RGO activated PS oxidation processes. To further investigate the combined role of RGO and PS in the non-radical oxidation process methanol quenching experiments were conducted without the addition of PS in T-RGO and the results are shown in Figure 10 (a) and (b). The degradation decreases drastically from 78 to 18% in the case of T-RGO system in 30 min. These varying responses of the two systems with the radical scavenger are clear indications of the non-radical oxidation pathways in T-RGO/PS system.

The zigzag edges on the graphene surface are believed to be the active sites to mediate the different oxidation pathways. When electron rich molecules approach the activated PS molecule, the possibility of formation of a ternary system of electron donor-mediator-acceptor was reported by Tang et al. [8]. Here, carbon network in RGO can act as an electron transfer mediator. The activated persulfate molecules are capable of oxidising an electron rich organic pollutant directly on the surface of RGO *via* extracting electrons from the substrate without producing reactive radicals (Eq. 17) [8].

$$S_2O_8^{2-} + 2e^{-1} \rightarrow 2SO_4^{2-} \quad (17)$$

This process remarkably enhances the efficiency of DCF removal. In this system, both radical and non-radical oxidation processes are simultaneously taking place for the complete degradation of DCF. Based on the above results, a mechanism involving both radical and non-radical reaction pathways is proposed and schematically shown in Figure 11.

3.2.5. Reuse of T-RGO photocatalyst

The application of all photocatalytic processes has close relation to the performance and long term stability of the catalysts. The scope for the reuse of a catalyst is essential from the environmental and economic aspects. In this context, the reusability of the T-RGO catalyst was investigated. Accordingly, after each photocatalytic experiment the catalyst was washed with deionized water, filtered, dried at 100 °C and reused. The performance and stability of the photocatalyst were studied for 5 operation cycles and the results are shown in Figure 12. For the first 3 trials the nanocomposite performed without any loss in efficiency. However, there is a marginal decrease in activity on subsequent use. In any case the activity of the catalyst decreases only very slowly, which indicates that it can be recycled multiple times.

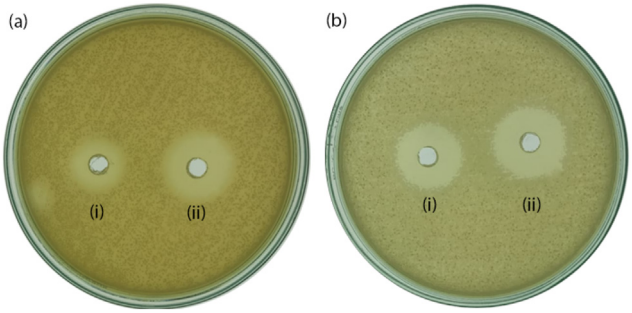

Figure 13. Photographs of the zone of inhibition of T-RGO and T-RGO/PS system by the well diffusion assay: (a) *E. coli* (i)T-RGO (ii) T-RGO/PS system (b) *S. aureus* (i) T-RGO (ii) T-RGO/PS system.

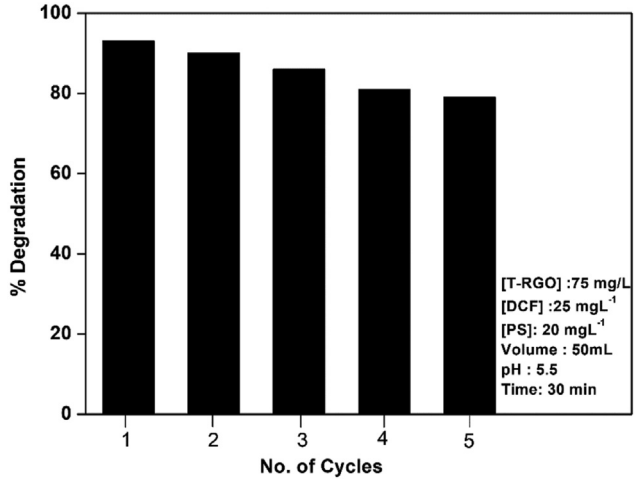

Figure 12. Effect of recycling of the catalyst on the efficiency of DCF degradation.

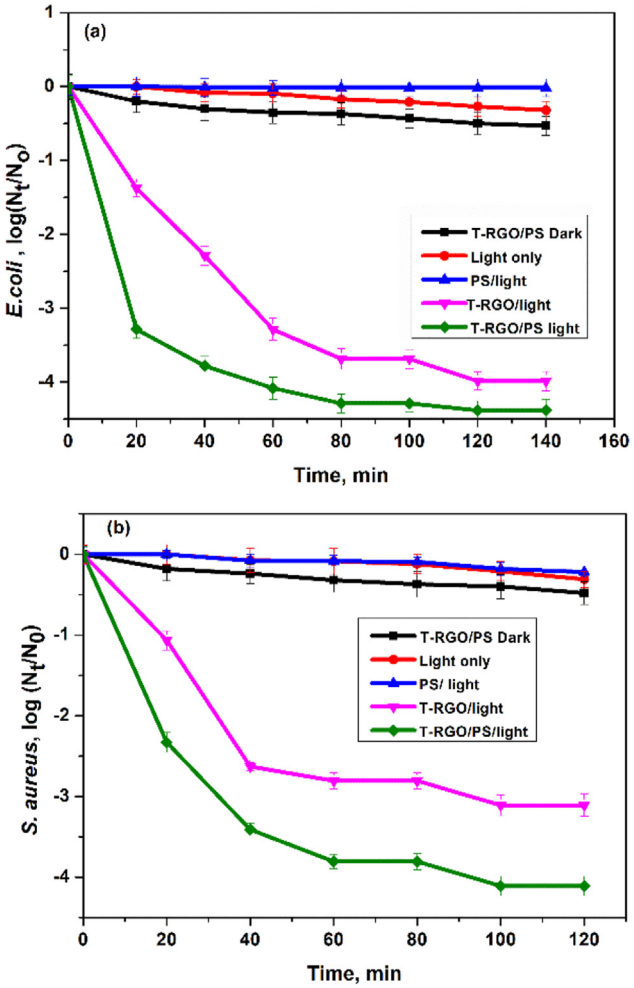

Figure 14. Photocatalytic inactivation of bacteria under visible LED light (a) *E. coli* (b) *S. aureus*.

A notable advantage of using T-RGO catalyst is that it is easy to filter and separate from the reaction system. Thus the use of T-RGO successfully solved the problem of recycling traditional TiO_2 catalysts which are creating secondary pollution.

3.3. Antibacterial activity

3.3.1. Evaluation of the antibacterial activity of T-RGO and T-RGO/PS systems

The well diffusion assay was used to get a first-hand qualitative evaluation of the inherent antimicrobial activity of the T-RGO and T-RGO/PS systems without light irradiation. Figure 13 shows the zone of inhibition obtained in the case of T-RGO and T-RGO/PS systems towards the representative bacteria under study. A slight enhancement is shown in the activity by T-RGO/PS system compared to T-RGO even in dark conditions. Pristine TiO_2 and PS alone are not showing any appreciable antibacterial activity in the dark.

In order to examine the photocatalytic antibacterial activity of the T-RGO and T-RGO/PS systems under visible light irradiation, the colony count method was adopted and the results are shown in Figure 14 (a) & (b). The enhanced photocatalytic inactivation is clearly evident from the results plotted. The bacteria showed a low degree of inactivation in the dark and light only conditions (during 120 min time period selected for the study). It is also demonstrated that the antibacterial activity is enhanced in a commendable manner on incorporation of PS in the system. In the case of *E. coli*, 80 min are needed for a 4 log removal with T-RGO/PS system. Without PS the removal rate is almost stabilized at 120 min with a 3 log removal. Compared to *E. coli* less inactivation is shown by *S. aureus*. However, the PS activation is more pronounced in the case of *S. aureus* where it has taken 100 min for a 4 log removal whereas without PS the removal rate nearly stabilized before achieving a 3 log removal. The effect of PS alone in visible light was also evaluated and no substantial effect over light alone was observed.

The enhanced activity of T-RGO/PS integrated system over T-RGO can be attributed to the increased production of ROS including the highly oxidising $SO_4^{\cdot-}$ radical anions as explained in section 3.2. The so formed ROS can exert oxidative stress in the microbial organisms in a number of ways. To begin with, the ROS can attack the peptidoglycan layer of the cell wall leading to the peroxidation of the phospholipid and oxidation of the protein membrane. This will disrupt cell wall causing the leakage of K^+ ions and other intracellular materials. ROS entering inside the cell will damage the cell functions primarily by altering/inhibiting the protein sequence for DNA replication by reacting with the sugar-phosphate group [38]. ROS attack on the coenzymes inhibiting the respiratory

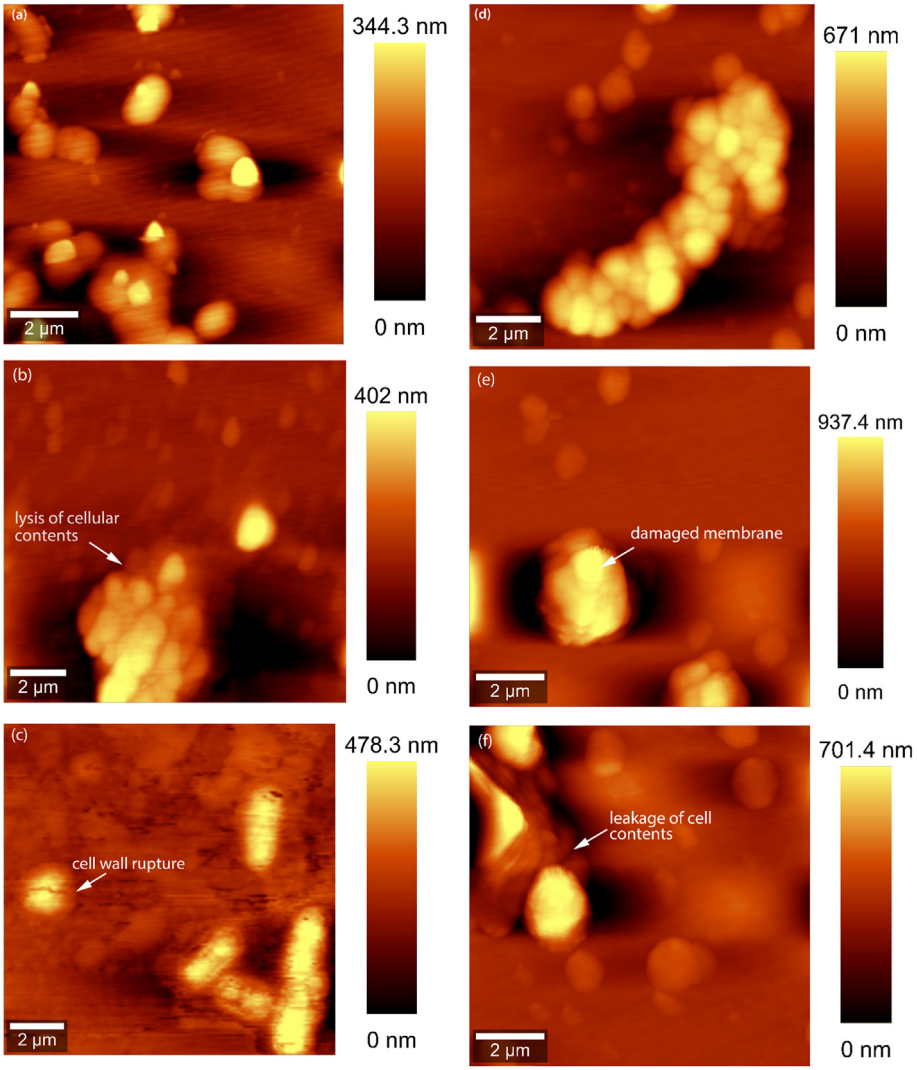

Figure 15. Morphological changes of bacterial cells. AFM images (a) *E. coli* control (b) after exposure to T-RGO/light (c) after exposure to T-RGO/PS/light (d) *S. aureus* control (e) after exposure to T-RGO/light (f) after exposure to T-RGO/PS/light.

functions of the microbes has also been reported [39]. In short, ROS mediated cell lysis can be generally represented by Eq. (18) [40].

$$\text{Microbial organisms in water} \xrightarrow{OH/SO_4^{-} \text{ and other ROS}} \text{Aliphatic acids} \quad (18)$$

3.3.2. Morphological changes of bacterial cells after exposure to T-RGO and T-RGO/PS treatment

T-RGO and T-RGO/PS systems effectively inactivated the microbes. The morphological changes of the cells before and after photocatalytic treatment were evaluated using AFM performed in tapping mode. As the aim of the study was to investigate the damage to bacterial morphology induced by photocatalytic treatment the results are mostly confined to the images obtained. From Figure 15, it can be seen that the rod like cells of *E. coli* and the cocci shaped clusters of *S. aureus* are damaged with cell wall disruption and possible cytoplasm leakage. The three-dimensional topographies are given in Fig. S7(Supplementary Material). These images clearly show the reduction in the number of cells after the treatment. Surface roughness values of the AFM images of *E. coli* and *S. aureus* cells shown in Figure 15 (a), (b), (c), (d), (e) and (f) are 66.583, 82.583, 366.014, 86.260, 105.211 and 151.629 nm respectively. It is seen that surface roughness increases after the treatment. Apart from oxidative stress by ROS, the other contributing factor to bacterial inactivation is the membrane stress exerted by the nanoparticles.

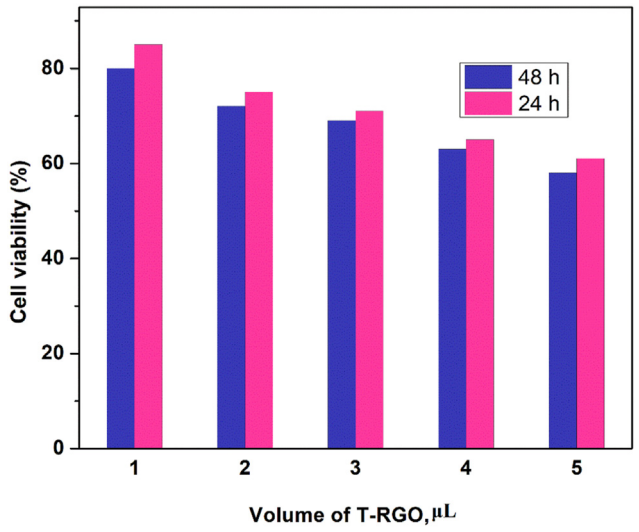

Figure 16. Cell viability assay of human macrophage cell towards T-RGO (1 mg/mL).

The physico-chemical properties of the T-RGO composite have a significant influence in this regard. The synthesised T-RGO is solely of anatase phase which is established to be more favourable for photocatalytic activity. Again it has been reported by several authors that the decrease in particle size as well as increased surface area would increase the surface interactions with the bacteria and hence antibacterial activity [41]. Moreover, the mesoporosity along with narrow pore size distribution also act as other favourable factors for the better antimicrobial activity. In this case the presence of extremely nanosized (4–5 nm) TiO_2 particles and the increased surface area could be accountable for its antimicrobial behaviour. The smaller sized particles as well as the sharp zigzag edges of graphene can penetrate deep into the cell membranes. The increased surface area could help to wrap the microbes thus arresting their growth. The better adhesion, penetration and the consequent leakage of intracellular materials are the major causes for the inherent antimicrobial activity of the composite.

To summarise, the enhanced antimicrobial activities of T-RGO and T-RGO/PS systems under visible light depend on the nanoscale distribution of particles, their structure, surface properties and characteristics of the individual components. The adhesion/deposition of the microbes on the surface of the material will enable good interfacial contact between these. As a result, a good wrapping of cells by RGO sheets prevents cell proliferation causing the loss of cell viability. The zigzag edge planes of graphene as well as the sharp sides of TiO_2 can trigger non porous piths on the cell surface leading to cytoplasm leakage and cell death. The oxidative degradation of the microbes caused by the reaction with highly reactive ROS is mainly accounted for the enhanced antibacterial activity under visible light.

3.3.3. Re-emergence

One of the major issues associated with deactivation of bacteria using light irradiation without the application of chemical disinfectants, is the re-emergence of bacterial growth, after switching off the light source. This may be due to the incomplete bacterial deactivation. The bacteria can transform to a viable non-cultural state which can regain its culturability under favourable conditions. The possibility of such re-emergence of the organism is examined by measuring the bacterial concentration after the visible light source has been put off. The deactivation continued

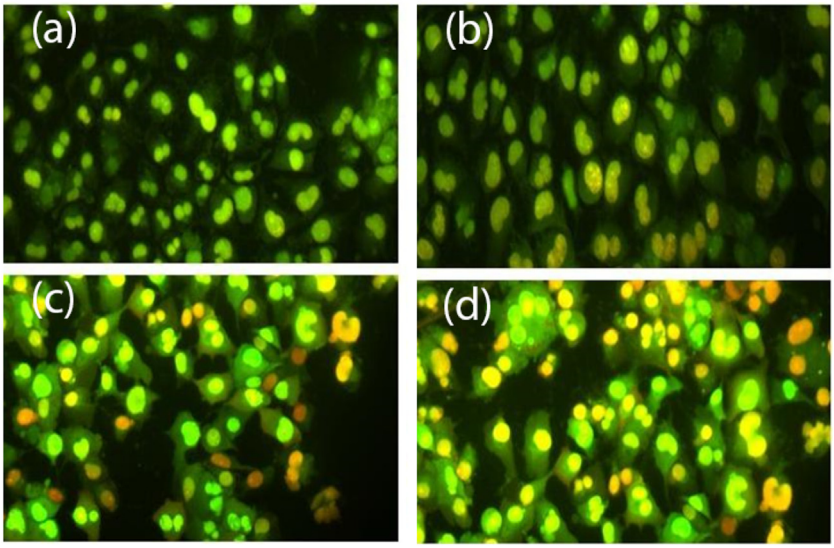

Figure 17. Live/Dead images of macrophages treated with T-RGO nanocomposite (1 mg/mL): Effect of dosages (a) control (b) 2 µL (c) 4 µL (d) 6 µL.

for some more time after the irradiation is discontinued, possibly because the free radicals generated in the process continue to be active for some more time until they are totally consumed by various processes taking place. In this case, no significant re-emergence is noticed even after 16 h. Hence, the destruction can be considered complete and irreversible in this case.

3.4. Cytotoxicity of T-RGO nanocomposites in human macrophage cell lines

Toxic nature of nanoparticles can lead to high risk in the treatment of water. Hence a comprehensive understanding about the toxicity of these materials is necessary in order to decide their applications. So the cytotoxicity of the prepared T-RGO nanocomposite is evaluated using MTT Cell Viability Assay and Metabolic Activity Assay.

Cell viability of human macrophage cells was investigated using the MTT assay. Cell viability after 24 h and 48 h of treatment were determined. Figure 16 shows the cell viability (%) of macrophage cells at different time intervals with respect to different doses of T-RGO. As evident from the figure, T-RGO shows very low toxicity at lower doses and toxicity increases with increase in dose. On increasing the volume from 1 μL to 5 μL the viability percentage decreases from 98 to 61. At lower doses even after 48 h the cell lines are active and the death ratio is less. This indicates that the toxicity of T-RGO nanocomposite is dose dependent and the catalyst is biocompatible and nontoxic at the dosage used in this study (75 mg/L).

Figure 17 shows the live/dead images of macrophages treated with T-RGO (1 mg/mL) obtained by the metabolic activity assay. The results are in accordance with the MTT assay, most of the cells are metabolically active. However, on increasing the dose a few of the cells are seen dead. These results suggest that T-RGO nanocomposite is not affecting the macrophages at lower concentrations and is biocompatible towards human macrophage cell lines.

4. Conclusions

A hybrid method involving two most frequently accepted AOPS, *viz.*, PS oxidation and T-RGO mediated heterogeneous photocatalysis is employed to remove the emerging pharmaceutical pollutant DCF. The enhanced photocatalytic performance of the synthesised T-RGO nanocomposite is attributed to the high crystallinity, exclusive anatase phase, the increased surface area, the finer dispersion of TiO_2 particles on the graphene sheet, reduced electron - hole recombination and extended visible light response. T-RGO composite is able to activate persulfate under sunlight. By combining PS oxidation process with T-RGO mediated photocatalysis, a DCF removal efficiency of more than 98% is achieved within 30 min. The degradation follows Langmuir-Hinshelwood mechanism and pseudo-first order kinetics. The pseudo-first order rate constant calculated for T-RGO/PS system is ~2 times higher than that of T-RGO. The DCF degradation is feasible at all pH levels. Radical scavenging experiments are conducted to ascertain the mechanism of degradation. In addition to a radical mechanism, a non-radical pathway involving the direct oxidation of DCF is also proposed. The complete mineralisation of DCF is confirmed by monitoring TOC which almost disappeared within 60 min.

The efficiency of this system for the photocatalytic inactivation of two representative bacteria under visible light is also investigated. Compared to T-RGO, T-RGO/PS system shows enhanced photocatalytic inactivation which is ascertained by the colony count method and the AFM images of the bacteria taken after treatment. The high oxidative attacks on bacteria by the increased amounts of ROS generated in the combined treatment are responsible for the enhanced photocatalytic antibacterial properties of T-RGO/PS system. The membrane disruption of the bacteria occurring due to the specific physico-chemical properties of the material may also be a major reason for the antibacterial activity of the studied systems. Investigation of cytotoxicity of T-RGO nanocomposite towards human macrophage cell lines indicates that the dose used in this study is safe for the treatment of water.

Declarations

Author contribution statement

Deepthi John: Conceived and designed the experiments; Performed the experiments; Analyzed and interpreted the data; Wrote the paper.

Sarita G Bhat: Contributed reagents, materials, analysis tools or data.

Jiya Jose: Performed the experiments; Analyzed and interpreted the data.

V Sivanandan Achari: Conceived and designed the experiments; Analyzed and interpreted the data; Contributed reagents, materials, analysis tools or data.

Funding statement

This research did not receive any specific grant from funding agencies in the public, commercial, or not-for-profit sectors.

Data availability statement

Data included in article/supplementary material/referenced in article.

Declaration of interests statement

The authors declare no conflict of interest.

Additional information

Supplementary content related to this article has been published online at https://doi.org/10.1016/j.heliyon.2021.e07451.

References

[1] Á. Tolosana-moranchel, A. Manassero, M.L. Satuf, O.M. Alfano, J.A. Casas, A. Bahamonde, Influence of TiO_2-rGO optical properties on the photocatalytic activity and efficiency to photodegrade an emerging pollutant, Appl. Catal. B Environ. 246 (2019) 1–11.

[2] T. Zhang, Y. Chen, Y. Wang, J. Le Roux, Y. Yang, J. Croue, Efficient peroxydisulfate activation process not relying on sulfate radical generation for water pollutant degradation, Environ. Sci. Technol. 48 (10) (2014).

[3] X. Duan, H. Sun, J. Kang, Y. Wang, S. Indrawirawan, S. Wang, Insights into heterogeneous catalysis of persulfate activation on dimensional-structured nanocarbons, ACS Catal. 5 (8) (2015) 4629–4636.

[4] F. Ghanbari, M. Moradi, Application of peroxymonosulfate and its activation methods for degradation of environmental organic pollutants: Review, Chem. Eng. J. 310 (2016) 41–62.

[5] J. Wang, S. Wang, Activation of persulfate (PS) and peroxymonosulfate (PMS) and application for the degradation of emerging contaminants, Chem. Eng. J. 334 (2018) 1502–1517.

[6] X. Chen, B. Yang, P. Oleszczuk, Y. Gao, X. Yuan, W. Ling, M. Gatheru, Vanadium oxide activates persulfate for degradation of polycyclic aromatic hydrocarbons in aqueous system, Chem. Eng. J. 364 (2019) 79–88.

[7] J. Chen, W. Hong, T. Huang, Activated carbon fiber for heterogeneous activation of persulfate: implication for the decolorization of azo dye, Environ. Sci. Pollut. Res. 18 (2016) 18564–18574.

[8] L. Tang, Y. Liu, J. Wang, G. Zeng, Y. Deng, H. Dong, H. Feng, J. Wang, B. Peng, Enhanced activation process of persulfate by mesoporous carbon for degradation of aqueous organic pollutants: electron transfer mechanism, Appl. Catal. B Environ. 231 (5) (2018) 1–10.

[9] X. Duan, Z. Ao, L. Zhou, H. Sun, G. Wang, S. Wang, Occurrence of radical and nonradical pathways from carbocatalysts for aqueous and nonaqueous catalytic oxidation, Appl. Catal. B Environ. 188 (2016) 98–105.

[10] N. Genç, E. Durna, E. Gengeç, Heterogeneous activation of persulfate by graphene oxide-TiO_2 nanosheet for oxidation of diclofenac : optimization by central composite design, Water, Air Soil Pollut 229 (2018) 330.

[11] X. Duan, Z. Ao, H. Sun, S. Indrawirawan, Y. Wang, J. Kang, F. Liang, Z.H. Zhu, S. Wang, Nitrogen-doped graphene for generation and evolution of reactive radicals by metal-free catalysis, ACS Appl. Mater. Interfaces 7 (2015) 4169–4178.

[12] W.S. Wang, D.H. Wang, W.G. Qu, L.Q. Lu, W. Xu, Large ultrathin anatase TiO_2 nanosheets with exposed {001} facets on graphene for enhanced visible light photocatalytic activity, J. Phys. Chem. C 116 (2012) 19893–19901.

[13] H. Zhang, X. Wang, N. Li, J. Xia, Q. Meng, J. Ding, J. Lu, Synthesis and characterization of TiO_2/graphene oxide nanocomposites for photoreduction of heavy metal ions in reverse osmosis concentrate, RSC Adv. 8 (2018) 34241–34251.
[14] D. John, A.S. Rajalekshmi, R.M. Lopez, V.S. Achari, TiO_2-reduced graphene oxide nanocomposites for the trace removal of diclofenac, SN Appl. Sci. (2020).
[15] D. John, Synthesis, Characterization and Testing of TiO_2-Reduced Graphene Oxide Nanocomposites for the Photocatalytic Removal of Pollutants from Water, Doctoral Thesis submitted to Cochin University of Science and Technoloy, Kochi, India, 2021.
[16] Y. Zhang, N. Zhang, Z. Tang, Y. Xu, Graphene transforms wide band gap ZnS to a visible light photocatalyst. The new role of graphene as a macromolecular photosensitizer, ACS *Nano* 6 (11) (2012) 9777–9789.
[17] Y. Chang, X. Ou, G. Zeng, J. Gong, C. Deng, Y. Jiang, J. Liang, G. Yuan, H. Liu, X. He, Synthesis of magnetic graphene oxide–TiO2 and their antibacterial properties under solar irradiation, Appl. Surf. Sci. 343 (2015) 1–10.
[18] Y.F. Dufrêne, Atomic force microscopy, a powerful tool in microbiology, J. Bacteriol. 184 (2002) 5205–5213.
[19] A. Stylianou, S. Kontomaris, C. Grant, E. Alexandratou, Atomic Force Microscopy on Biological Materials Related to Pathological Conditions, Scanning, 2019. Article ID 8452851.
[20] A. Knoll, R. Magerle, G. Krausch, Tapping mode atomic force microscopy on polymers: where is the true sample surface? Macromolecules 34 (2001) 4159–4165.
[21] T.A. Camesano, M.J. Natan, B.E. Logan, Observation of changes in bacterial cell morphology using tapping mode atomic force microscopy, Langmuir 16 (2000) 4563–4572.
[22] T. Mosamann, Rapid colorimetric assay for cellular growth and survival: application to proliferation and cytotoxicity assays, J. Immunol. Methods 65 (1983) 55–63.
[23] S. Francis, S. Joseph, E.P. Koshy, B. Mathew, Microwave assisted green synthesis of silver nanoparticles using leaf extract of elephantopus scaber and its environmental and biological applications, Artif Cells Nanomed Biotechnol 46 (2018) 795–804.
[24] W.F. Zhang, Y.L. He, M.S. Zhang, Z. Yin, Q. Chen, Raman scattering study on anatase TiO_2 nanocrystals, J. Phys. D Appl. Phys. 33 (2000) 912–916.
[25] S. Stankovich, D.A. Dikin, R.D. Piner, K.A. Kohlhaas, A. Kleinhammes, Y. Jia, Y. Wu, S.T. Nguyen, R.S. Ruoff, Synthesis of graphene-based nanosheets via chemical reduction of exfoliated graphite oxide, Carbon 45 (2007) 1558–1565.
[26] Y. Wang, W. Duan, B. Liu, X. Chen, F. Yang, J. Guo, The effects of doping copper and mesoporous structure on photocatalytic properties of TiO_2, J. Nanomater. (2014). Article ID 178152.
[27] J. Sun, H. Zhang, L.-H. Guo, L. Zhao, Two-dimensional interface engineering of a titania-graphene nanosheet composite for improved photocatalytic activity, Appl. Mater. Interfaces 5 (2013) 13035–13041.
[28] T. Nguyen-phan, V. Hung, E. Jung, E. Oh Hyun, J. Suk, B. Lee, E. Woo, Reduced graphene oxide-titanate hybrids: morphologic evolution by alkali-solvothermal treatment and applications in water purification, Appl. Surf. Sci. 258 (2012) 4551–4557.
[29] J.F. Leal, S.M.A. Cruz, B.T.A. Almeida, V.I. Esteves, P.A.A.P. Marques, E.B.H. Santos, TiO_2-rGO nanocomposite as an efficient catalyst to photodegrade formalin in aquaculture's waters, under solar light, Environ. Sci.: Water Res. Technol. 6 (2020) 1018–1027.
[30] M.P. Nikhila, A.K. Akhila, T. Divya, M. Anju, T.V.A. Kusumam, N.K. Renuka, P123 and solvent assisted synthesis of titania nanocuboids with co-exposed {101} and {001} planes, CrystEngComm 19 (2017) 511–518.
[31] L.W. Matzek, K.E. Carter, Activated persulfate for organic chemical degradation: a review, Chemosphere 151 (2016) 178–188.
[32] T. Olmez-hanci, I. Arslan-alaton, S. Gurmen, I. Gafarli, S. Khoei, S. Safaltin, D.Y. Ozcelik, Oxidative degradation of bisphenol A by carbocatalytic activation of persulfate and peroxymonosulfate with reduced graphene oxide, J. Hazard Mater. 360 (2018) 141–149.
[33] A. Georgi, F. Kopinke, Interaction of adsorption and catalytic reactions in water decontamination processes Part I . Oxidation of organic contaminants with hydrogen peroxide catalyzed by activated carbon, Appl. Catal. B Environ. 58 (2005) 9–18.
[34] J. Sun, M. Song, J. Feng, Y. Pi, Highly efficient degradation of ofloxacin by UV/Oxone/Co^{2+} oxidation process, Environ. Sci. Pollut. Res. 19 (2012) 1536–1543.
[35] C.M. Park, J. Heo, D. Wang, C. Su, Y. Yoon, Heterogeneous activation of persulfate by reduced graphene oxide-elemental silver/magnetite nanohybrids for the oxidative degradation of pharmaceuticals and endocrine disrupting compounds in water, Appl. Catal. B Environ. 225 (2018) 91–99.
[36] T.A. Khan, E.A. Khan, Shahjahan, Adsorptive uptake of basic dyes from aqueous solution by novel brown linseed deoiled cake activated carbon : equilibrium isotherms and dynamics, J. Environ. Chem. Eng. 4 (2016) 3084–3095.
[37] R. Xiao, Z. Luo, Z. Wei, S. Luo, R. Spinney, W. Yang, D.D. Dionysiou, Activation of peroxymonosulfate/persulfate by nanomaterials for sulfate radical-based advanced oxidation technologies, Curr. Opin. Chem. Eng. 19 (2018) 51–58.
[38] I. Matai, A. Sachdev, P. Dubey, S.U. Kumar, B. Bhushan, P. Gopinath, Antibacterial activity and mechanism of Ag-ZnO nanocomposite on S . aureus and GFP-expressing antibiotic resistant E . coli, Colloids Surf., B 115 (2014) 359–367.
[39] P. Ganguly, C. Byrne, A. Breen, S.C. Pillai, Antimicrobial activity of photocatalysts : fundamentals , mechanisms , kinetics and recent advances, Appl. Catal. B Environ. 225 (2018) 51–75.
[40] A. Rincón, C. Pulgarin, Effect of pH , inorganic ions , organic matter and H_2O_2 on E . coli K12 photocatalytic inactivation by TiO_2: implications in solar water disinfection 51 (2004) 283–302.
[41] L. Zhang, Y. Jiang, Y. Ding, M. Povey, D. York, Investigation into the antibacterial behaviour of suspensions of ZnO nanoparticles (ZnO nanofluids), J. Nanoparticle Res. 9 (2007) 479–489.